Check for updates

ADVANCED FUNCTIONAL MATERIALS
www.afm-journal.de

High-Performance Infrared Photodetectors Driven by Interlayer Exciton in a Van Der Waals Epitaxy Grown HfS_2/MoS_2 Vertical Heterojunction

*Minkyun Son, Hanbyeol Jang, Dong-Bum Seo, Ju Hyeok Lee, Jin Kim, Minsu Kim, Saewon Kang, Soonmin Yim, Wooseok Song, Jung-Woo Yoo, Hyun You Kim, Sun Sook Lee, and Ki-Seok An**

The van der Waals (vdW) heterojunctions of transition metal dichalcogenides (TMDCs) provide an advanced platform for interlayer exciton generation to detect the exceeding cutoff wavelengths of individual TMDCs. Herein, the first demonstration of high-performance infrared (IR) photodetectors driven by interlayer excitons and based on HfS_2/MoS_2 vdW heterojunctions grown by chemical vapor deposition is presented. HfS_2 exhibits selective growth only on MoS_2, establishing a vertical heterojunction that effectively generates interlayer excitons. The synthesized HfS_2/MoS_2 vertical heterojunction with type-II band alignment exhibits a low interlayer bandgap and a significantly large interface area, enabling highly efficient IR detection. Moreover, the built-in potential in HfS_2/MoS_2 plays a pivotal role in the outstanding photoresponse by suppressing the dark current and providing gradient band bending for the interlayer exciton-induced photocarriers to drift toward each electrode. The HfS_2/MoS_2 photodetector exhibits remarkable performance, achieving a detectivity (D^*) of $\approx 7 \times 10^{13}$ Jones at 1550 nm, D^* of $\approx 2 \times 10^{14}$ Jones at 980 nm, and fast response time of 60 µs, surpassing previously reported 2D photodetectors. Overall, the successful demonstration of a photodetector based on vdW epitaxial HfS_2/MoS_2 paves the way for the advancement of large-scale high-performance IR sensors.

1. Introduction

Infrared (IR) photodetectors are important for a wide range of civilian and military applications, including modern scientific studies, engineering production, geological prospecting, medical examinations, nighttime imaging, chemically specific remote sensing, and photon counters in photonic quantum computers.[1–4] The demand for high-performance IR sensors is on the rise, as required by advancements in application devices. However, in the near future, the commercialization of photodetectors based on InGaAs and Si will encounter significant challenges, such as lattice mismatch between the semiconductor material and the mother substrate.[5–7]

2D semiconductors exhibit exotic properties such as the absence of dangling bonds and the ability to form van der Waals (vdW) bonds with other materials, offering a distinct advantage over conventional semiconductors.[8–10] These remarkable benefits have led to many reports on high-performance photodetectors based on vdW heterojunctions of 2D semiconductors with clean interfaces induced by vdW gaps.[10,11] However, most photodetectors based on vdW heterojunctions focus on detecting visible light.[12,13] Although there have been several reports on IR detection in recent years, a significant challenge remains owing to the issue of high dark currents in such devices.[10,12,14] The trade-off between low dark current and the detection of long wavelengths, imposed

M. Son, H. Jang, D.-B. Seo, J. Kim, M. Kim, S. Kang, S. Yim, W. Song, S. S. Lee, K.-S. An
Thin Film Materials Research Center, Korea Research Institute of Chemical Technology
141 Gajeong-ro, Yuseong-gu, Daejeon 34114, Republic of Korea
E-mail: ksan@krict.re.kr

The ORCID identification number(s) for the author(s) of this article can be found under https://doi.org/10.1002/adfm.202308906

© 2023 The Authors. Advanced Functional Materials published by Wiley-VCH GmbH. This is an open access article under the terms of the Creative Commons Attribution-NonCommercial License, which permits use, distribution and reproduction in any medium, provided the original work is properly cited and is not used for commercial purposes.

DOI: 10.1002/adfm.202308906

M. Son, J.-W. Yoo
Department of Materials Science and Engineering
Ulsan National Institute of Science and Technology
50 UNIST-gil, Ulju-gun, Ulsan 44919, Republic of Korea

J. H. Lee, H. Y. Kim
Department of Materials Science and Engineering
Chungnam National University
99 Daehak-ro, Yuseong-gu, Daejeon 34134, Republic of Korea

M. Kim
Department of Advanced Materials Engineering
Kyonggi University
154-42 Gwanggyosan-ro, Gyeonggi-do, Suwon 16227, Republic of Korea

 © 2023 The Authors. Advanced Functional Materials published by Wiley-VCH GmbH

by the small bandgap necessary for IR detection, is a major hurdle for achieving low-noise photodetectors.[15]

Recently, a novel approach was introduced in the form of IR detectors that operate by interlayer excitons within a vdW heterojunction to overcome the aforementioned issue.[16–19] vdW heterojunctions with a type-II band alignment formed by transition metal dichalcogenides (TMDCs) offer an advanced platform for generating interlayer excitons, enabling the detection of wavelengths that exceed the cutoff limits of individual TMDCs.[10,17,19] Interlayer excitons in vdW heterojunctions arise from the Coulomb interaction between electrons and localized holes.[20,21] The spatial segregation of excitons across two distinct layers leads to advantageous characteristics, including broadening of the photoresponse wavelength, enhancement in exciton lifetime, and generation of an oriented nonzero electric dipole moment with mutually repulsive interactions.[16] These unique characteristics of interlayer excitons present new avenues for designing high-performance optoelectronic devices that eliminate the trade-off between low dark currents and the detection of long wavelengths.[10,16] A few reports have presented promising IR photodetectors powered by interlayer excitons.[10,17,22,23] However, the devices based on mechanically exfoliated flakes are limited to unit devices.[10,17,22,23]

Herein, we present the first demonstration of high-performance IR photodetectors that operate by interlayer excitons and are fabricated based on vdW heterojunctions grown by chemical vapor deposition (CVD), marking a significant milestone in the field of optoelectronic devices. We selected a heterojunction platform utilizing a combination of HfS_2 and MoS_2 as the interlayer exciton-driven IR detector. This was motivated by the selective growth of HfS_2 and the appropriate band offsets of HfS_2 and MoS_2.[24–26] In our two-step CVD process, HfS_2 exhibited selective growth only on MoS_2, allowing for the establishment of a vertical heterojunction with a substantial interface area and providing favorable conditions for the generation of interlayer excitons. In addition, the conduction band edge of HfS_2 is located at 5.2 eV which is a large value compared with other TMDs.[27,28] Therefore, the difference between the conduction band edge of HfS_2 and the valence band edge of MoS_2 is small, enabling the formation of an interlayer bandgap that is sufficiently narrow for IR detection.[26,28]

Furthermore, the significant contribution of the built-in potential within the HfS_2/MoS_2 heterojunction was instrumental in achieving exceptional photoresponse in the HfS_2/MoS_2 photodetector. This built-in potential effectively suppresses the dark current and facilitates gradient band bending, enabling an efficient drift of the interlayer exciton-induced photocarriers toward the respective electrodes. Our HfS_2/MoS_2 photodetector exhibits remarkable performance, achieving a photoresponsivity (R) of ≈600 A W^{-1}, detectivity (D^*) of $\approx 7 \times 10^{13}$ Jones at 1550 nm, and R of ≈1500 A W^{-1} and D^* of $\approx 2 \times 10^{14}$ Jones at 980 nm. Additionally, the photodetector exhibited fast rise and decay times of 60 and 71 µs, respectively.

2. Results and Discussion

Figure 1a illustrates the procedure for synthesizing a vdW vertical heterojunction of HfS_2 and MoS_2 using a two-step method. We previously reported a synthetic method for obtaining large-grain MoS_2 through CVD assisted by an alkali metal halide (AMH).[29] Briefly, in the first step, a mixture of an AMH (NaCl) and a metal source (MoO_3) is deposited onto a SiO_2/p-Si substrate through thermal evaporation. This mixture served as a reactant for the formation of large-grained MoS_2.[29] Subsequently, the deposited mixture is placed inside a quartz tube and reacts with sulfur at a temperature of 750 °C. The synthesized MoS_2 flakes, which act as the platform for HfS_2 synthesis, exhibit a flake size of ≈200 µm with a coverage of 86% (Figure 1a inset). The synthesized MoS_2 with significant grain sizes can offer ample space as a platform for the creation of numerous nucleation sites. Additionally, it facilitates effective adsorption and diffusion of Hf and S sources on the MoS_2 surface, allowing the synthesis of HfS_2 at these nucleation sites.[30,31] The second step involved a catalyst-assisted CVD method for growing vdW epitaxy-based HfS_2 on MoS_2. NaCl and $HfCl_4$ powders were used at a fixed mass ratio of 1:3 (NaCl:$HfCl_4$). The sources reacted under an Ar and H_2 atmosphere at 760 Torr/950 °C on the synthesized MoS_2.

Figure 1b and Figure S1 (Supporting Information) present the scanning electron microscopy (SEM) and the optical image of the synthesized HfS_2/MoS_2 heterojunctions. In the SEM image, hexagonal HfS_2 is clearly observed on the surface of the MoS_2. The average grain size of the HfS_2 is 6.75 µm, as shown in Figure 1c. Although the size of each individual HfS_2 is only a few micrometers, they merge with one another, resulting in the formation of numerous large-area regions, leading to an HfS_2 coverage of ≈79% on the MoS_2 substrate. In addition, a small amount of bulk HfS_2 is synthesized along the grain boundaries of MoS_2, where the surface energy is relatively high.[32] Moreover, to demonstrate the uniform synthesis of HfS_2 across various locations on the MoS_2 substrate, we present four SEM images of HfS_2/MoS_2 taken at different positions (Figure S2a–d, Supporting Information). In all four SEM images, the presence of hexagonally structured HfS_2 is evident. Although there may be slight variations in HfS_2 coverage, it is observable that a predominant layer of a few HfS_2 layers has been consistently synthesized on all MoS_2 surfaces. The thickness profile of HfS_2 in the inset of Figure 1b reveals that the HfS_2 flakes formed on the MoS_2 substrate had a thickness of 3.5 nm, corresponding to five layers of HfS_2. The SEM image clearly shows that HfS_2 exhibits a preference for specific substrates. Notably, HfS_2 hardly grew on the SiO_2 region but only on the MoS_2 substrate. This intriguing selectivity can be attributed to the disparity in the surface energy associated with the surface diffusion of reactants, which is influenced by the morphological characteristics of the respective mother substrates.[31]

The growth of HfS_2 by CVD involves two primary steps: First, the vaporized reactants are deposited onto the mother substrate, and second, the adsorbed species undergo diffusion on the mother substrate.[31] During the synthesis of HfS_2 at high temperatures, the migration rate of the reactant molecules was higher on the MoS_2 substrate than on the SiO_2 substrate.[31] This was attributed to the absence of dangling bonds in MoS_2, which facilitated faster migration.[31] The enhanced migration rate provided sufficient time for the adsorbed HfS_2 molecules to achieve a minimum energy state, promoting the growth of HfS_2 on the MoS_2 substrate by lowering the cohesive energy.[31] To quantitatively compare the cohesive energy of HfS_2/MoS_2 and HfS_2/SiO_2, we employed density functional theory (DFT)

© 2023 The Authors. Advanced Functional Materials published by Wiley-VCH GmbH

16163028, 2024, 7, Downloaded from https://onlinelibrary.wiley.com/doi/10.1002/adfm.202308906 by Ulsan National Institute Of, Wiley Online Library on [23/04/2024]. See the Terms and Conditions (https://onlinelibrary.wiley.com/terms-and-conditions) on Wiley Online Library for rules of use; OA articles are governed by the applicable Creative Commons License

16163028, 2024, 7, Downloaded from https://onlinelibrary.wiley.com/doi/10.1002/adfm.202308906 by Ulsan National Institute Of, Wiley Online Library on [23/04/2024]. See the Terms and Conditions (https://onlinelibrary.wiley.com/terms-and-conditions) on Wiley Online Library for rules of use; OA articles are governed by the applicable Creative Commons License

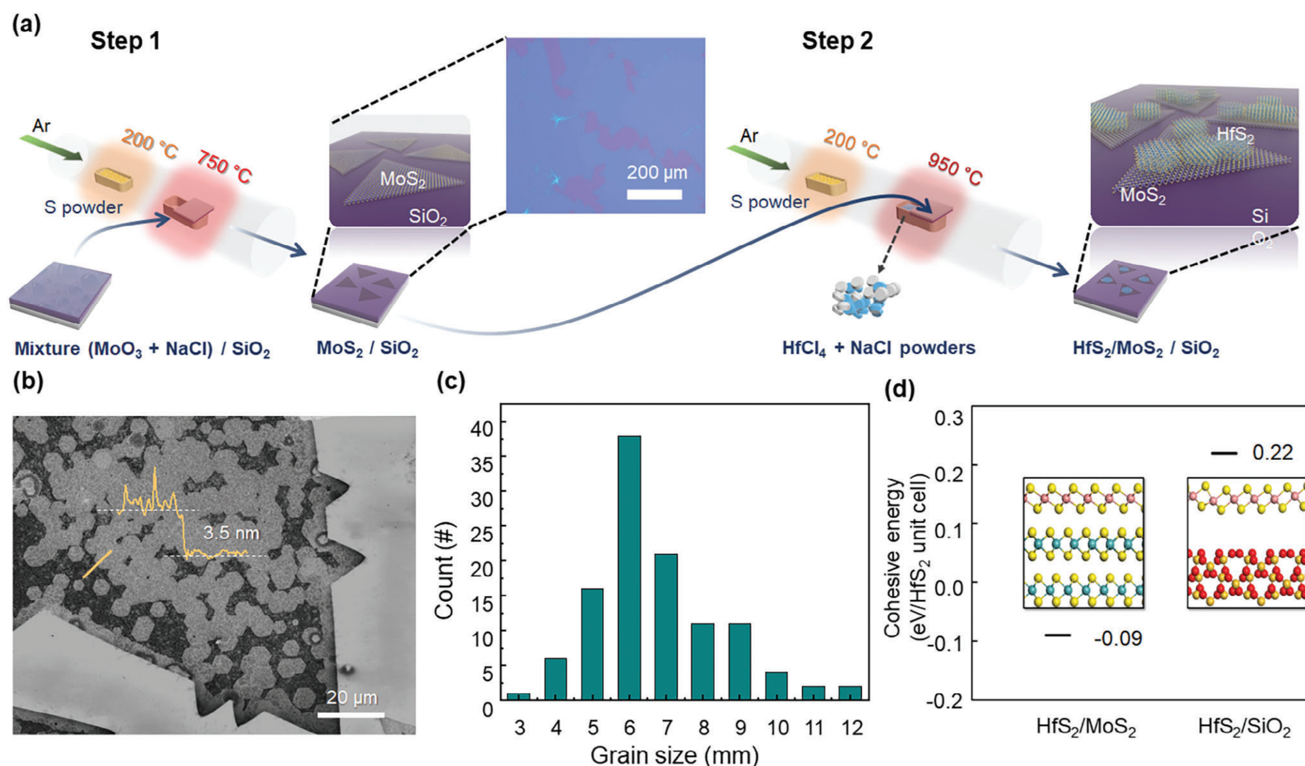

Figure 1. a) Schematic of overall two-step HfS_2/MoS_2 synthesis procedures. The Inset image is a synthesized MoS_2 and the scaler bar denotes 200 μm. b) SEM image and (inset) thickness profile of synthesized HfS_2/MoS_2 and the scaler bar denotes 20 μm. c) Distribution of HfS_2 hexagons grain size from SEM. d) Calculated cohesive energy per HfS_2 unit cell of HfS_2/MoS_2 and HfS_2/SiO_2.

calculations to theoretically calculate the cohesive energy. The theoretical models are shown in Figure 1d. The value of cohesive energy is calculated using the formula $E_{\text{cohesive}} = (E_{\text{HfS2}}/\text{sub} - E_{\text{HfS2}} - E_{\text{sub}})/n$, where $E_{\text{HfS2}}/\text{sub}$, E_{HfS2}, E_{sub}, and n represent the total energy of HfS_2/MoS_2 or HfS_2/SiO_2, HfS_2, MoS_2, or SiO_2, the number of HfS_2 units in the HfS_2/MoS_2 or HfS_2/SiO_2.[31] The results of the DFT calculations reveal that the cohesive energies of HfS_2/MoS_2 and HfS_2/SiO_2 structures are −0.09 and 0.22 eV, respectively, as shown in Figure 1d. The cohesive energy of HfS_2/SiO_2 is over zero, and a significant cohesive energy difference of 0.31 eV is observed between HfS_2/SiO_2 and HfS_2/MoS_2. This energy difference clearly explains the selective growth of HfS_2 on the MoS_2 substrate. Despite the growth of HfS_2 exhibiting selectivity, when the substrate is exposed to excessive metal sources, bulk HfS_2 with a grain size of less than 1 μm can be observed on SiO_2, as shown in Figure S3 (Supporting Information). This is because the high temperature required for synthesizing HfS_2 allows some of the remaining reactants not to participate in the formation of HfS_2/MoS_2 to overcome the cohesive energy of HfS_2/SiO_2.[31] Furthermore, under the same conditions, the coverage of few-layer HfS_2 and bulk HfS_2 on the MoS_2 substrate also increased (Figure S3, Supporting Information) due to the excessive metal sources. In our two-step CVD process, HfS_2 grew selectively exclusively on MoS_2, leading to the formation of a vertical heterojunction with a significant interface area, which was beneficial for generating interlayer excitons.

Raman spectroscopy and photoluminescence (PL) were employed to investigate the structural and optical properties of pristine MoS_2 and HfS_2/MoS_2, as shown in **Figure 2**a–c. In the Raman spectrum of pristine MoS_2 (Figure 2a), two characteristic Raman peaks are observed at 384.2 and 403.4 cm^{-1}, corresponding to the E^1_{2g} and A_{1g} vibrational modes, respectively.[26,33] The E^1_{2g} peak exhibits a small full width at half maximum of 3.9 cm^{-1}, and there is a peak-to-peak distance of 19.2 cm^{-1} between E^1_{2g} and A_{1g}. These observations indicate that the synthesized monolayer MoS_2 exhibits a quality comparable to that of the flakes exfoliated from bulk single crystals.[26,33] After HfS_2 synthesis, a noticeable blue shift is observed in the A_{1g} mode while the position of the E^1_{2g} vibration mode exhibits a relatively small difference (Figure S4, Supporting Information). This shift suggests that MoS_2 is *p*-doped because of the junction with HfS_2, which has a higher Fermi level than MoS_2.[33] Additionally, the out-of-plane mode A_{1g} peak exhibited a more pronounced shift than the in-plane mode E^1_{2g} peak, which can be attributed to the growth of HfS_2 on the MoS_2 surface.[33] Furthermore, comparing MoS_2 in the region where HfS_2 was not synthesized and the pristine MoS_2 subsequent to HfS_2 synthesis, one can observe nearly no shift in the vibration mode. This indicates that there are no additional defects generated in MoS_2, and Hf doping doesn't take place during the high-temperature growth of HfS_2.[34] Therefore, the high-quality state of MoS_2 is preserved evidently (Figure S5, Supporting Information). The Raman spectra of the HfS_2/MoS_2 heterostructure also exhibit a distinct vibrational mode of HfS_2 at 335 cm^{-1}.[24,25] In the case of few-layer HfS_2/MoS_2, the intensity of the HfS_2 Raman signal is significantly lower compared to

 © 2023 The Authors. Advanced Functional Materials published by Wiley-VCH GmbH

16163028, 2024, 7, Downloaded from https://onlinelibrary.wiley.com/doi/10.1002/adfm.202308906 by Ulsan National Institute Of, Wiley Online Library on [23/04/2024]. See the Terms and Conditions (https://onlinelibrary.wiley.com/terms-and-conditions) on Wiley Online Library for rules of use; OA articles are governed by the applicable Creative Commons License

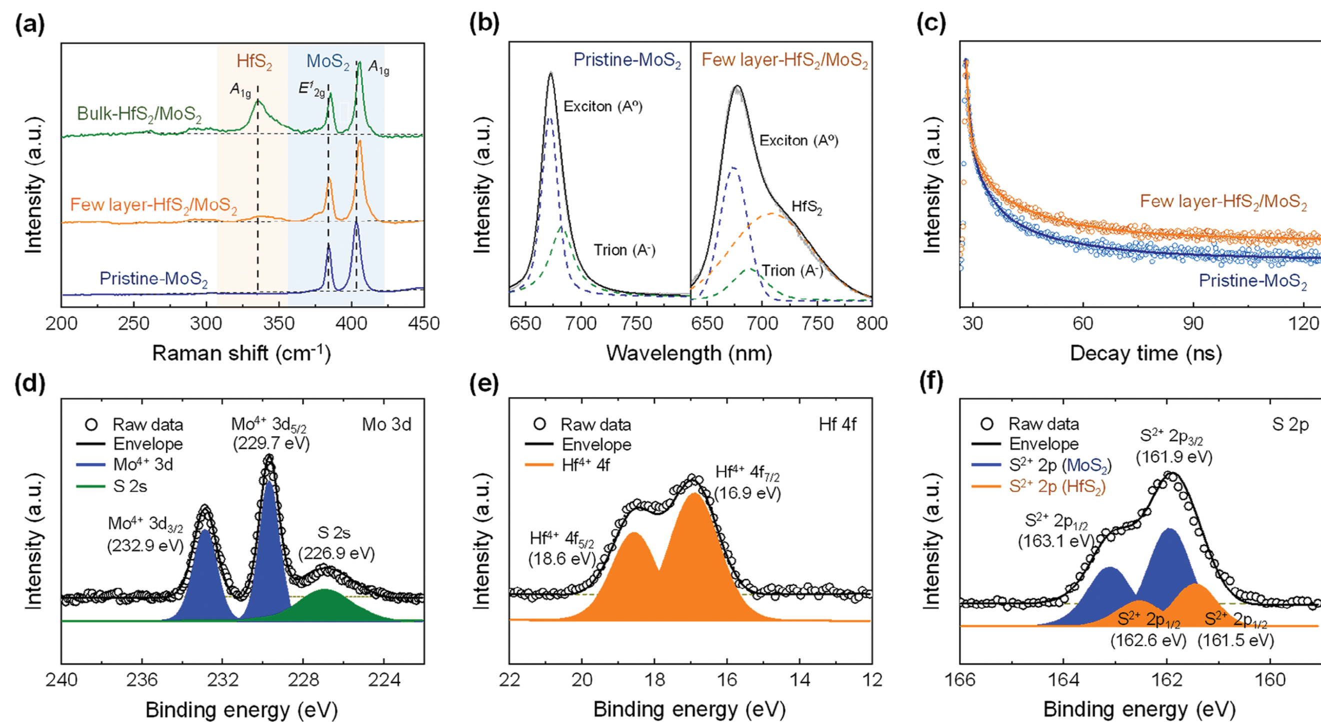

Figure 2. a) Raman spectra of bulk HfS_2/MoS_2, few layer HfS_2/MoS_2, and pristine MoS_2. b) PL spectra of few layer HfS_2/MoS_2 and pristine MoS_2. c) TRPL spectra of HfS_2/MoS_2 and MoS_2, d) Mo 3d and S 2s, e) Hf 4f, and f) S 2p XPS spectra of HfS_2/MoS_2.

bulk HfS_2/MoS_2, which can be attributed to the reduction in the number of scattering centers within the HfS_2 structure.[24,25] Furthermore, to validate the consistent quality of HfS_2, we conducted Raman spectroscopy at positions corresponding to Figure 1a and Figure S2a–e (Supporting Information). In the Raman spectra, we observed the low-intensity $A^1{}_g$ mode of HfS_2 across all the few HfS_2 layers synthesized, irrespective of their position on the MoS_2 substrate (as shown in Figure 2a). This demonstrates a uniform quality of HfS_2 layers synthesized on MoS_2. This implies that the HfS_2/MoS_2 heterojunction, synthesized through our two-step CVD process, has achieved a consistent quality sufficient for potential future device array production.

A comparison of the PL spectra of pristine MoS_2 and few-layer HfS_2/MoS_2 is shown in Figure 2b. The PL spectrum of pristine MoS_2 exhibited a prominent peak at 680 nm, corresponding to the exciton (A°, blue) and trion (A^-, green) emissions.[33] In contrast, the PL spectrum of the HfS_2/MoS_2 heterostructure revealed the presence of an additional subcurve (orange) with a peak at 715 nm. The observed HfS_2 PL peak position is in line with the previous study.[35] However, many publications indicate peak positions that vary from this specific peak.[24,25,36] The peak position does not match numerous publications that indicate distinct peak positions. This variance is attributed to defects arising during the synthesis of HfS_2.[35] This peak position falls within the range reported for CVD-grown few-layered HfS_2.[24,25,36] The PL curve of HfS_2/MoS_2 displays a decrease of the intensity ratio of $A^-/A°$ from 0.38 (MoS_2) to 0.24 (HfS_2/MoS_2) compared to that of pristine MoS_2.[33,37] This phenomenon can be attributed to *p*-doping, wherein electrons are transferred from MoS_2 to HfS_2, as agreed with the Raman analysis.[33,37] Moreover, the PL peak intensity of HfS_2/MoS_2 heterostructure is significantly lower than that of pristine MoS_2 (Figure S6, Supporting Information), which was attributed to the reduced recombination of the photogenerated carriers through HfS_2/MoS_2 heterojunction.[38,39] To further analyze the optical properties, time-resolved PL measurements were performed, as shown in Figure 2c. The PL decay curves were measured at the peak positions in the PL spectra. The average lifetime extracted from Figure 2c is prolonged in HfS_2/MoS_2 compared to that in pristine MoS_2. This suggests that the HfS_2/MoS_2 heterojunction reduces nonradiative recombination in MoS_2 and has more compatibility for enhanced efficiency of separating photoinduced electron–hole pairs, which is consistent with the PL results.[38–41]

Based on the aforementioned Raman and PL spectroscopy results, we conclude that the HfS_2/MoS_2 heterojunction was synthesized via a two-step CVD process. To further elucidate the chemical composition of the heterostructure, chemical identification of HfS_2/MoS_2 was implemented by X-ray photoelectron spectroscopy (XPS) measurements (Figure 2d–f; Figure S7, Supporting Information). The XPS profiles of the Mo 3d, Hf 4f, S 2s, and S 2p core levels of the HfS_2/MoS_2 heterojunction are shown in Figure 2d–f. In Figure 2d, the deconvoluted peak profiles indicate the presence of Mo $3d_{5/2}$ and Mo $3d_{3/2}$ orbitals in intrinsic MoS_2, as well as S 2s orbitals in MoS_2.[24,25,29,33] These profiles demonstrate the absence of Mo 3d and MoS_x orbitals in the defective MoS_2 and MoO_x.[42] Furthermore, no signals corresponding to the Na and Cl orbitals, which are contaminants from the catalyst used in the synthesis process, were observed (Figure S8, Supporting Information). These results suggest that pristine MoS_2 synthesized using the AMH-assisted CVD method

© 2023 The Authors. Advanced Functional Materials published by Wiley-VCH GmbH

16163028, 2024, 7, Downloaded from https://onlinelibrary.wiley.com/doi/10.1002/adfm.202308906 by Ulsan National Institute Of, Wiley Online Library on [23/04/2024]. See the Terms and Conditions (https://onlinelibrary.wiley.com/terms-and-conditions) on Wiley Online Library for rules of use; OA articles are governed by the applicable Creative Commons License

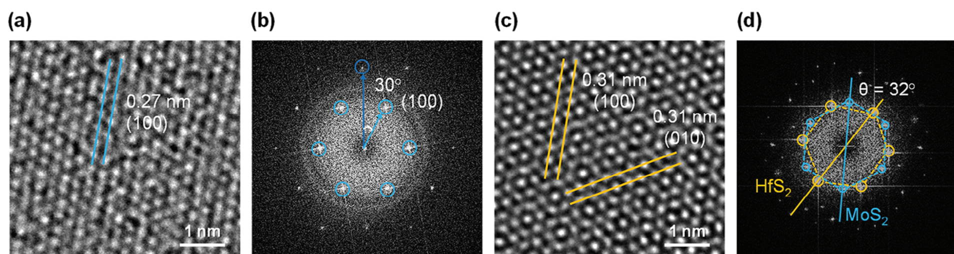

Figure 3. a,b) Top view HRTEM image and corresponding FFT analysis of MoS_2. c,d) HRTEM image of HfS_2/MoS_2 heterojunction with moiré patterns and corresponding FFT analysis. The scaler bar denotes 1 nm.

is of high quality and devoid of structural defects and undesirable impurities. In Figure 2e, distinct peaks corresponding to the Hf $4f_{5/2}$ and Hf $4f_{7/2}$ orbitals are observed at 18.6 and 16.9 eV, respectively, indicating the presence of HfS_2 without any detectable HfO_x orbitals.[24,25] The XPS spectra in the range of 160–165 eV for S 2p orbitals exhibit deconvoluted peak profiles at 162.6 and 161.5 eV for HfS_2, and 163.1 and 161.9 eV for MoS_2, as shown in Figure 2f.[24,25] By comparing the areas of the S 2p (MoS_2, blue)/Mo 3d and S 2p (HfS_2, orange)/Hf 4f orbitals, the stoichiometry of MoS_2 and HfS_2 can be determined. The ratios of these areas provided stoichiometries are 1.98:1 (S:Mo) for MoS_2 and 2.01:1 (S:Hf) for HfS_2. Comparing it with the atomic ratio of Mo and S in pristine MoS_2 (S:Mo = 1.97:1), we observe nearly negligible differences (Figure S9, Supporting Information). Therefore, XPS analysis showed the clear orbitals of MoS_2 and HfS_2 and confirmed the presence of high-quality HfS_2/MoS_2 without additive defects in MoS_2 and Hf doping.

To confirm directly the presence of a vertical heterojunction between HfS_2 and MoS_2, high-resolution transmission electron microscopy (HRTEM) images and corresponding fast Fourier transform (FFT) analyses were obtained, as shown in **Figure 3**. The HRTEM image (Figure 3a) and selected area electron diffraction (SAED) pattern (Figure 3b) show the presence of high-quality 2H-MoS_2 monolayers.[29] In Figure 3c,d, the HRTEM image reveals a hexagonal structure of Hf atoms, with crystal distances of 0.31 nm corresponding to the (100) and (110) planes.[24] In the folded region of the HfS_2/MoS_2 heterojunction, five distinguishable layers were observed at the folding boundary, with a layer distance of 0.59 nm, consistent with the previously reported lattice information of HfS_2 (Figure S10, Supporting Information).[24] The thickness information of HfS_2 obtained from HRTEM complements the thickness profile obtained from atomic force microscopy analysis, further confirming the accurate thickness of HfS_2. Additionally, Figure 3c shows the moiré patterns induced by the overlapping of 2H MoS_2 and 1T HfS_2 at a rotation angle of 32°.[43] The dominant moiré pattern is characterized by a hexagonal arrangement, with six Hf atoms surrounding a central Hf atom.[43] Moreover, Figure S11a (Supporting Information) shows a variety of moiré patterns (depicted in orange, red, and blue), and it is clear that these patterns align accurately in both shape and position with those portrayed in the TEM image (Figure S11, Supporting Information). The rotation angle can be observed in the heterojunction of the 1T/2H structure, which also reveals that HfS_2 is freestanding on MoS_2.[43] Moreover, the rotation angle extracted from the HRTEM image is similar to the stacking angles observed in SEM images (Figure S12, Supporting Information). The stacking angles of the heterojunctions exhibit low disorientation between 1T HfS_2 and 2H MoS_2, suggesting the minimal presence of MoS_2 wrinkles or contamination at the interface.[44] These results provide clear evidence of a vertical heterojunction between 1T HfS_2 and 2H MoS_2, confirming the epitaxial growth of HfS_2 on MoS_2. This epitaxial growth without undesirable contamination is favorable for generating a large number of photoinduced carriers at the interface between HfS_2 and MoS_2.

A schematic (optical image) of a photodetector based on HfS_2/MoS_2 is presented in **Figure 4**a (Figure S13, Supporting Information). To exploit the asymmetric energy band structure of the epitaxially grown HfS_2/MoS_2 vertical heterojunction, we strategically aligned the drain and source electrodes on MoS_2 and HfS_2, respectively. Figure 4b shows the characteristics of drain current (I_{DS}) versus drain voltage (V_{DS}) for the HfS_2/MoS_2 photodetector in the dark and under the illumination of different incident light powers (P = 0.2—500 μW cm^{-2}). In the dark, the device exhibited similar electrical properties regardless of the polarity of V_{DS}, indicating no significant difference in the energy barrier between the source and drain, even in the presence of a heterojunction (Figure S14, Supporting Information). However, in the case of the optoelectrical properties, the photocurrent ($I_{ph} = I_{light}–I_{dark}$) and the ratio of I_{light} to I_{dark} (I_{light}/I_{dark}) of the device, where I_{light} and I_{dark} denote I_{DS} under illumination and in the dark, respectively, exhibited noticeable differences at V_{DS} = −5 V compared to V_{DS} = 5 V, as depicted in Figure 4b,c. The value of I_{ph} increases as the incident P increases, following the relationship $I_{ph} \approx P^{\alpha}$.[45] The power factor ($\alpha$), which represents the efficiency of photodetection, is more than 10 times higher at V_{DS} = −5 V compared to at V_{DS} = 5 V under visible light illumination (470, 532, and 625 nm), as shown in Figure S15 (Supporting Information).[45] The asymmetric photodetection efficiency of our photodetector by the polarity of V_{DS} will be comprehensively discussed in the subsequent paragraph with additional details.

The band alignment of the HfS_2/MoS_2 photodetector in V_{DS} direction is shown in Figure S16 (Supporting Information) to explain in more detail about difference of the optoelectrical properties by V_{DS} polarity. The electron affinity values of HfS_2 and MoS_2 were reported as 5.2 and 3.9 eV, respectively, and the bandgaps of HfS_2 and MoS_2 were determined from the PL spectra.[26,28] As shown in Figure S16 (Supporting Information), when V_{DS} is negative, gradient band bending occurs in the device, allowing photoinduced electrons from both MoS_2 and HfS_2 to readily flow toward the respective electrodes. The presence of this band bending facilitates the significant contribution of

© 2023 The Authors. Advanced Functional Materials published by Wiley-VCH GmbH

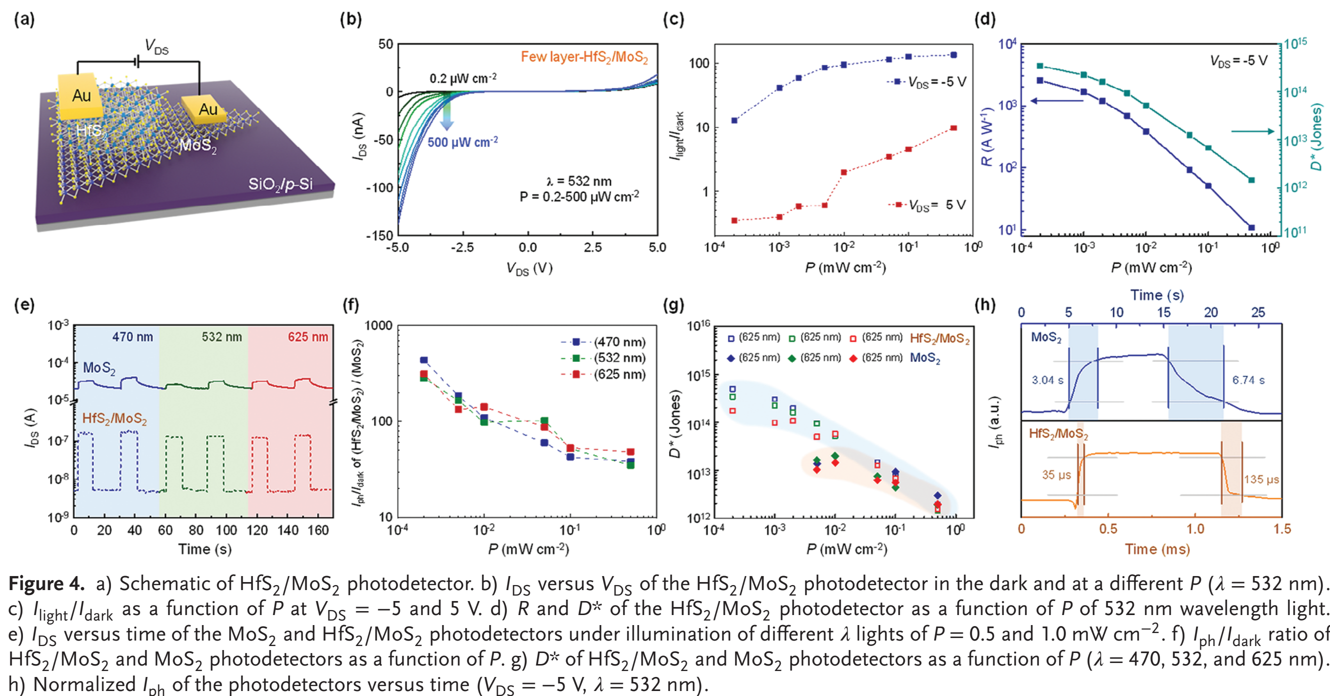

Figure 4. a) Schematic of HfS_2/MoS_2 photodetector. b) I_{DS} versus V_{DS} of the HfS_2/MoS_2 photodetector in the dark and at a different P ($\lambda = 532$ nm). c) I_{light}/I_{dark} as a function of P at $V_{DS} = -5$ and 5 V. d) R and D^* of the HfS_2/MoS_2 photodetector as a function of P of 532 nm wavelength light. e) I_{DS} versus time of the MoS_2 and HfS_2/MoS_2 photodetectors under illumination of different λ lights of $P = 0.5$ and 1.0 mW cm^{-2}. f) I_{ph}/I_{dark} ratio of HfS_2/MoS_2 and MoS_2 photodetectors as a function of P. g) D^* of HfS_2/MoS_2 and MoS_2 photodetectors as a function of P ($\lambda = 470$, 532, and 625 nm). h) Normalized I_{ph} of the photodetectors versus time ($V_{DS} = -5$ V, $\lambda = 532$ nm).

photoelectrons to the overall photocurrent. Conversely, in the positive V_{DS} regime, an energy barrier was formed at the interface between MoS_2 and HfS_2, impeding the transfer of photoinduced electrons from HfS_2 to MoS_2. Furthermore, the main channel for photoelectrons differs depending on the polarity of V_{DS}, with HfS_2 being the main channel at a negative V_{DS} and MoS_2 at a positive V_{DS}. This distinction arises from the different directions of charge transfer associated with the polarity of V_{DS}. Notably, the mobility of HfS_2 was more than four times that of MoS_2.[46] The high drift velocity of the photoelectrons, determined by the high carrier mobility of the main channel, allows sufficient transit time for the photoelectrons to reach the electrode before recombination occurs owing to scattering effects.[47]

To compare the photoelectric properties of the HfS_2/MoS_2 photodetectors based on the carrier mobility of the main channel, Figure S17 (Supporting Information) shows the ratio of I_{ph} at $V_{DS} = -5$ V to I_{ph} at $V_{DS} = 5$ V (I_{ph}–-5 V / I_{ph}–5 V) as a function of P. The ratio of I_{ph} increases with increasing P in the range of 0.2—50 μW cm^{-2}. This behavior can be attributed to the fact that in MoS_2, which has a low mobility, the scattering between the photoelectrons intensifies as the photocarrier density increases.[47,48] In contrast, in HfS_2, which has high mobility, scattering does not significantly increase because of the short transit time of the photoelectrons. However, the ratio of I_{ph} decreases in the range of 50—500 μW cm^{-2} owing to increased scattering in HfS_2, similar to the behavior observed in MoS_2. Therefore, the high photodetection efficiency at negative V_{DS} can be attributed to the high drift velocity of the photoelectrons in HfS_2, along with the presence of a gradient band. This is why our photodetector exhibited remarkable performance under a negative bias compared to a positive bias. The extracted photoresponsivity (R) and detectivity (D^*) of our photodetector as functions of P are shown in Figure 4d, where $R = I_{ph}/PA$, $D^* = RA^{1/2}/(2qI_{noise})^{1/2}$, A denotes the active area for photodetection, q denotes the electron charge, and I_{noise} denotes the I_{dark}.[26,40] We calculated detectivity by taking I_{dark} as I_{noise}. This is a method commonly used in many 2D materials based on photodetectors,[26,33,49,50] but at low frequencies (< few kHz), it is not white noise but G-R noise resulting from the trapping/de-trapping and generation/recombination processes of carriers within the active layer, and flicker ($1/f$) noise is dominant.[51–53] Therefore, the noise measured by the methods is underestimated and the detection performance of the device is also overestimated.[51–53] To obtain a correct value for I_{noise}, excluding flicker noise dominant at lower frequencies, a system to measure NEP is required.[54,55] However, due to the unavailability of such a system during the research, I_{dark} was utilized. The active area of our photodetector is 2500 μm^2 (width: 50 μm and length: 50 μm). Notably, our HfS_2/MoS_2 photodetector exhibits R values exceeding 2500 A W^{-1} and achieves D^* of ≈4 × 10^{14} Jones.

We fabricated the MoS_2 photodetector to compare its optoelectrical properties with those of the HfS_2/MoS_2 photodetector at $V_{DS} = -5$ V. Figure 4e–h shows that the optoelectrical properties of the HfS_2/MoS_2 and MoS_2 photodetectors were measured using excitation in the visible range (470, 532, and 625 nm). It was observed that both I_{dark} and I_{light} of the MoS_2 photodetector were significantly higher than those of the HfS_2/MoS_2 devices. This disparity can be attributed to the absence of a built-in potential in the MoS_2 photodetector, except for the junction at the MoS_2/electrode interface. In contrast, the HfS_2/MoS_2 photodetector exhibits reduced I_{dark} and I_{light} values because of the presence of an energy barrier that restricts the electron flow at the interface between HfS_2 and MoS_2, thereby minimizing the dark current to a few nanoamperes. Interestingly, the HfS_2/MoS_2 photodetector exhibited an unprecedented improvement in I_{ph}/I_{dark}, exceeding that of the MoS_2 photodetector by more than 100 times

© 2023 The Authors. Advanced Functional Materials published by Wiley-VCH GmbH

16163028, 2024, 7, Downloaded from https://onlinelibrary.wiley.com/doi/10.1002/adfm.202308906 by Ulsan National Institute Of, Wiley Online Library on [23/04/2024]. See the Terms and Conditions (https://onlinelibrary.wiley.com/terms-and-conditions) on Wiley Online Library for rules of use; OA articles are governed by the applicable Creative Commons License

16163028, 2024, 7, Downloaded from https://onlinelibrary.wiley.com/doi/10.1002/adfm.202308906 by Ulsan National Institute Of, Wiley Online Library on [23/04/2024]. See the Terms and Conditions (https://onlinelibrary.wiley.com/terms-and-conditions) on Wiley Online Library for rules of use; OA articles are governed by the applicable Creative Commons License

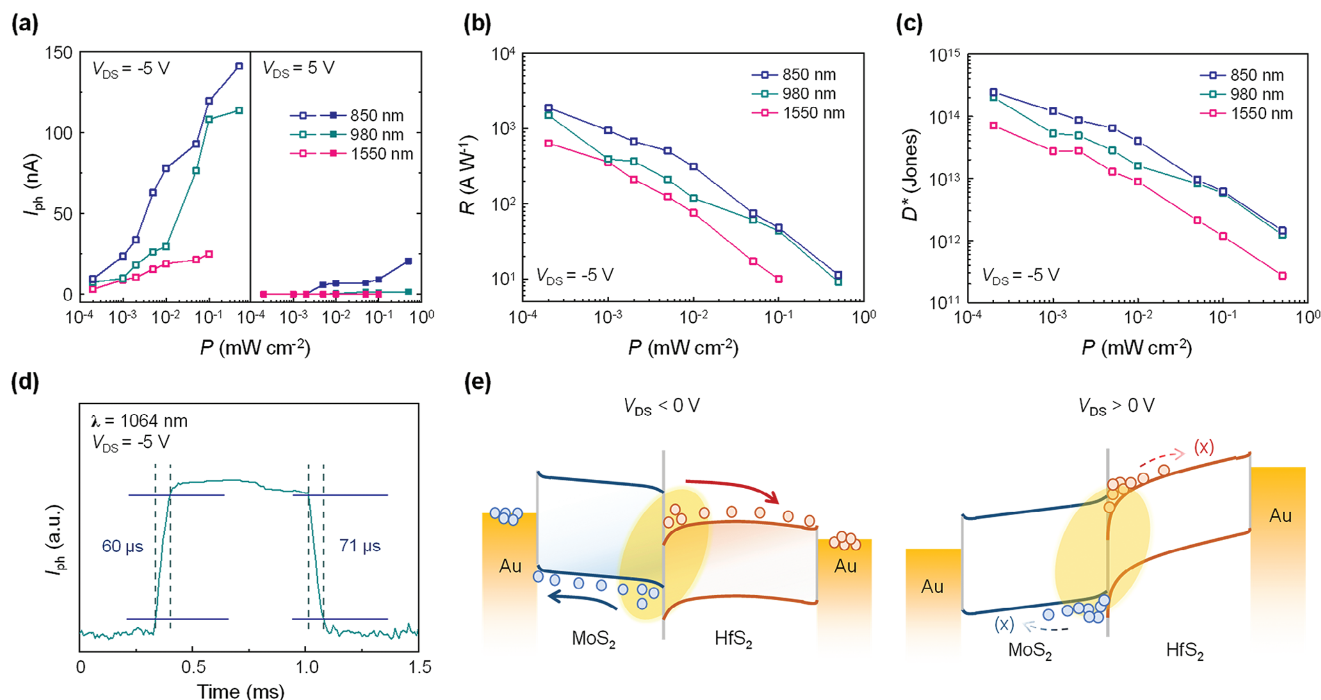

Figure 5. IR sensor based on HfS_2/MoS_2 driven by interlayer exciton. a) I_{ph} as a function of P at $V_{DS} = -5$ and 5 V ($\lambda = 850$, 980, and 1550 nm). b,c) R and D^* as a function of P under the illumination of 850, 980, and 1550 nm wavelength light ($V_{DS} = -5$ V). d) Normalized I_{ph} versus time ($\lambda = 1064$ nm). e) Schematic diagram of band alignment of the HfS_2/MoS_2 photodetector under $V_{DS} < 0$ V (left) and $V_{DS} > 0$ V (right) and the photoinduced carrier extraction process.

(Figure 4f). Moreover, the HfS_2/MoS_2 photodetector exhibited superior D^* at low P values compared with the MoS_2 photodetector. It achieved a D^* of $\approx 5 \times 10^{14}$ Jones under a low P, which MoS_2 alone cannot detect. These improvements are ascribed not only to the energy barrier of the HfS_2/MoS_2 interface that screens the injected carriers, inducing a low dark current but also to the junction with HfS_2, which possesses excellent optoelectronic properties.[46] The HfS_2/MoS_2 photodetector also exhibited an excellent response speed, as evidenced by its rapid rise and decay times, as shown in Figure 4h. These times were extracted based on the transitions from 10% to 90% of the maximum current and 90% to 10% of the current, respectively.[33] The HfS_2/MoS_2 photodetector achieves significantly shorter rise (35 μs) and decay times (135 μs) compared to both the MoS_2 and HfS_2/MoS_2 photodetectors operating with an applied $V_{DS} = 5$ V, where the main channel is formed by MoS_2 (Figure S18, Supporting Information).

The photoresponses of the HfS_2/MoS_2 photodetectors were also investigated at different IR wavelengths (850, 980, and 1550 nm). **Figure 5**a shows I_{ph} under illumination of IR light as a function of P at $V_{DS} = -5$ and 5 V. Under 850 nm wavelength light, the HfS_2/MoS_2 photodetector exhibits a remarkably high photocurrent at $V_{DS} = -5$ V than that at $V_{DS} = 5$ V, similar to the behavior observed in the visible light region. However, the HfS_2/MoS_2 photodetector exhibited no photoresponse at the wavelengths of 980 and 1550 nm at $V_{DS} = 5$ V. These behaviors of our photodetector suggest that the mechanism for generating photoinduced carriers differs depending on the wavelength. Figure 5b,c shows the R and D^* values of our photodetector versus P under illumination at 850, 980, and 1550 nm. The HfS_2/MoS_2 IR sensors exhibited outstanding performance at $V_{DS} = -5$ V, achieving an R value of ≈1500 A W^{-1} and D^* value of 2×10^{14} Jones at 980 nm, and R of ≈600 A W^{-1} and D^* of 7×10^{13} Jones at 1550 nm. Furthermore, the photoresponse time of the HfS_2/MoS_2 photodetector was evaluated under the illumination of a 1064 nm laser, as shown in Figure 5d. The rise and decay times were 60 and 71 μs, respectively, which are comparable to the photoresponse times observed under the illumination of a 532 nm laser. The performance characteristics of our HfS_2/MoS_2 photodetector surpass those of other previously reported CVD-grown 2D-based IR sensors (Tables S1 and S2, Supporting Information). The detectivity of our HfS_2/MoS_2 photodetector is several orders higher compared to the reported 2D materials based on photodetector, but considering the issue of overestimation mentioned above, it is difficult to directly compare the values. Nonetheless, upon comprehensive consideration of other performance metrics such as responsivity and response time, it becomes evident that our HfS_2/MoS_2 photodetector has reached a remarkable performance.

The generation of photoinduced carriers in the IR range involves two mechanisms: 1) electron-hole pair generation in HfS_2 and 2) interlayer exciton formation at the interface between HfS_2 and MoS_2. This is supported by the fact that the MoS_2 photodetector, which has a larger bandgap, could not detect IR signals (Figure S19, Supporting Information).[22] Figure 5e illustrates the process of photoinduced electron extraction by interlayer excitons in the band alignment of HfS_2/MoS_2 at $V_{DS} = -5$ and 5 V. At the interface of HfS_2/MoS_2, the generation of interlayer

© 2023 The Authors. Advanced Functional Materials published by Wiley-VCH GmbH

excitons under IR light illumination is possible because of the interlayer bandgap of 0.5 eV between the conduction band of HfS_2 and the valence band of MoS_2 (Figure S16, Supporting Information). In the negative V_{DS} region, the photoinduced electrons and holes from the interlayer excitons flow along HfS_2 and MoS_2, respectively, and can easily reach the respective electrodes owing to the applied electric field. In contrast, in the positive V_{DS} region, the photoinduced electrons and holes from the interlayer excitons move against the applied electric field toward the electrodes, limiting their contribution to the positive photocurrent. Consequently, the only mechanism responsible for the photoresponse of our photodetector under 980 and 1550 nm wavelength light is the generation and extraction of interlayer excitons, as no photoresponse was observed at $V_{DS} = 5$ V. In contrast, because our photodetector exhibits photodetection under 850 nm light even at $V_{DS} = 5$ V, a portion of the photocurrent arises from the excited photoinduced electrons in HfS_2. When HfS_2/MoS_2 detects light that each MoS_2 and HfS_2 cannot detect, the presence or absence of asymmetric photocurrent caused by bias polarity provides evidence that photocarriers resulting from interlayer excitation contribute to the photocurrent.[17] In particular, given the low likelihood of additional defects forming in the HfS_2/MoS_2 structure or Hf doping occurring in MoS_2, the sole source for photocarrier generation is interlayer excitation. Consequently, we have demonstrated a high-performance IR detector utilizing photocarriers generated through interlayer excitons in the CVD-synthesized HfS_2/MoS_2 structure.

3. Conclusion

In summary, we successfully demonstrated high-performance photodetectors based on a CVD-grown HfS_2/MoS_2 heterojunction. In our two-step CVD process, HfS_2 exhibited exclusive growth only on MoS_2, resulting in the establishment of a vertical heterojunction with a substantial interface area. This favorable configuration effectively promotes the generation of interlayer excitons. The interface between HfS_2 and MoS_2 exhibits an energy barrier, resulting in a low dark current, and the low interlayer bandgap enables the detection of IR signals by interlayer excitons. Through comprehensive chemical analyses, we confirmed the synthesis of high-quality epitaxial HfS_2/MoS_2 heterojunctions without defects or interface contamination using a two-step CVD method. The HfS_2/MoS_2 photodetector exhibited a remarkable performance, with a D^* of $\approx 5 \times 10^{14}$ Jones at a wavelength of 470 nm, representing a 36-fold improvement over the MoS_2 photodetector. Notably, at a wavelength of 1550 nm, which is beyond the detection range of the individual HfS_2 and MoS_2 channels, the HfS_2/MoS_2 photodetector achieved an R of ≈ 600 A W^{-1}, D^* of $\approx 7 \times 10^{13}$ Jones, and rapid rise and decay times of 60 and 71 µs, respectively. This interlayer exciton-driven IR sensor, which was first reported as a TMDC synthesized by CVD, opens up possibilities for the large-scale development of high-performance 2D IR sensors.

4. Experimental Section

Growth of MoS_2: CVD growth of MoS_2 was performed using a 2-inch tubular furnace. The process began with the preparation of a sample through the predeposition of MoO_3 and NaCl on a substrate, which was then placed in a crucible. The crucible was positioned at the center of the main heater. A crucible containing 4 g sulfur powder was placed upstream of the sample. The distance between the sulfur-filled crucible and the sample was set to 20 cm. Ar was used as the carrier gas, and the flux was maintained at 200 sccm throughout the experiment. The chamber was heated at a rate of 30 °C min^{-1} with a pressure maintained at 760 Torr by controlling the valve of the exhaust line. Once the temperature reached 150 °C, it was maintained for 15 min. Subsequently, the heating rate was reduced to 25 °C min^{-1} until a temperature of 500 °C was achieved. At this point, the heating zone of sulfur vaporized. Consequently, when the chamber temperature reached 750 °C, the temperature of the sulfur had increased by 200 °C. The main heater and heating zone of the sulfur were turned off after the temperature was maintained at 750 °C for 20 min. The system was then allowed to cool naturally.

Growth of HfS_2/MoS_2 Vertical Heterojunction: The growth of the vertical heterojunction was performed using a 1-inch tubular furnace. MoS_2 on SiO_2 was placed in a crucible at the center of the main heater. A mixture of $HfCl_4$ (0.02 g) and NaCl (0.01 g) was placed inside the crucible on the side farther from MoS_2. Upstream of the crucible, 4 g of sulfur was placed 15 cm from MoS_2. Throughout the process, a flow of H_2 gas (15 sccm) and Ar (20 sccm) gases were used. MoS_2 was heated at a rate of 30 °C min^{-1} until it reached 150 °C, which was then maintained for 15 min. The temperature was subsequently increased at a higher rate of 40 °C min^{-1} up to 500 °C. At this point, the sulfur heating zone was turned on. When the temperature of the main heater reached 950 °C, the sulfur heating zone reached 150 °C. These conditions were maintained for 30 min. The system was allowed to cool naturally, and the HfS_2/MoS_2 vertical heterojunction growth process was completed.

Characterization: Optical microscopy (BX53M, Olympus), Raman spectroscopy (InVia, Renishaw, 514 nm laser), PL measurement (UNINANOTECH, $\lambda_{ext} = 532$ nm), time-resolved PL (467 nm pulsed laser, Fluorolog 3, Horiba Scientific; time-correlated single-photon spectrometer), XPS (K-alpha, Thermo Fisher Scientific; Al Kα source at 1486.6 eV; pass energy: 50 eV), and AFM (Innova, Bruker) were used for pristine MoS_2 and HfS_2/MoS_2 heterojuntion characterization. For the TEM measurements, the HfS_2/MoS_2 heterojunction was transferred to a TEM grid (lacey carbon on an Au mesh) using a polystyrene-assisted transfer method. High-resolution TEM imaging was performed using a Cs-corrected TEM (HD-2300A, Hitachi). For the electrical/optoelectronic properties of MoS_2 and HfS_2/MoS_2, the source and drain electrodes were deposited by the thermal evaporation of Cr/Au (3/70 nm) and patterning with a shadow mask on MoS_2 and HfS_2/MoS_2. The electronic and optoelectronic properties of the devices were characterized using a semiconductor parameter analyzer (4200-SCS, Keithley) under vacuum (2 mTorr) using light-emitting diodes of various wavelengths (λ = 470, 530, 625, 850, 980, and 1550 nm). The high-speed photoresponse was measured using an oscilloscope and a current amplifier under 532 and 1064 nm wavelength laser, and the on- and off-states of the laser were modulated using a mechanical chopper.

Supporting Information

Supporting Information is available from the Wiley Online Library or from the author.

Acknowledgements

M.S., H.J., and D.-B.S. contributed equally to this work. This research was supported by the National Research Foundation of Korea (NRF) funded by the Ministry of Science and ICT (2021M3H4A3A01055854 and 2021M3H4A3A02099208).

Conflict of Interest

The authors declare no conflict of interest.

© 2023 The Authors. Advanced Functional Materials published by Wiley-VCH GmbH

16163028, 2024, 7, Downloaded from https://onlinelibrary.wiley.com/doi/10.1002/adfm.202308906 by Ulsan National Institute Of, Wiley Online Library on [23/04/2024]. See the Terms and Conditions (https://onlinelibrary.wiley.com/terms-and-conditions) on Wiley Online Library for rules of use; OA articles are governed by the applicable Creative Commons License

Data Availability Statement

The data that support the findings of this study are available in the supplementary material of this article.

Keywords

epitaxy growth, HfS_2/MoS_2, interlayer exciton, infrared sensors, vertical heterojunction

Received: July 31, 2023
Revised: October 12, 2023
Published online: November 1, 2023

[1] A. Tittl, A. Leitis, M. Liu, F. Yesilkoy, D.-Y. Choi, D. N. Neshev, Y. S. Kivshar, H. Altug, *Science* **2018**, *360*, 1105.
[2] H.-S. Zhong, H. Wang, Y.-H. Deng, M.-C. Chen, L.-C. Peng, Y.-H. Luo, J. Qin, D. Wu, X. Ding, Y. Hu, P. Hu, X.-Y. Yang, W.-J. Zhang, H. Li, Y. Li, X. Jiang, L. Gan, G. Yang, L. You, Z. Wang, L. Li, N.-L. Liu, C.-Y. Lu, J.-W. Pan, *Science* **2020**, *370*, 1460.
[3] R. Soref, *Nat. Photonics* **2010**, *4*, 495.
[4] L. Zhang, J. Ding, H. Zheng, S. An, H. Lin, B. Zheng, Q. Du, G. Yin, J. Michon, Y. Zhang, Z. Fang, M. Y. Shalaginov, L. Deng, T. Gu, H. Zhang, J. Hu, *Nat. Commun.* **2018**, *9*, 1481.
[5] T. Sasaki, K. Arafune, H. S. Lee, N. J. Ekins-Daukes, S. Tanaka, Y. Ohshita, M. Yamaguchi, *Phys. B Condens. Matter* **2006**, *376–377*, 626.
[6] T. Sasaki, K. Arafune, W. Metzger, M. J. Romero, K. Jones, M. Al-Jassim, Y. Ohshita, M. Yamaguchi, *Sol. Energy Mater. Sol. Cells* **2009**, *93*, 936.
[7] D. Liang, J. E. Bowers, *Nat. Photonics* **2010**, *4*, 511.
[8] M. Long, P. Wang, H. Fang, W. Hu, *Adv. Funct. Mater.* **2019**, *29*, 1803807.
[9] N. Huo, G. Konstantatos, *Adv. Mater.* **2018**, *30*, 1801164.
[10] W. Ahmad, J. Liu, J. Jiang, Q. Hao, D. Wu, Y. Ke, H. Gan, V. Laxmi, Z. Ouyang, F. Ouyang, Z. Wang, F. Liu, D. Qi, W. Zhang, *Adv. Funct. Mater.* **2021**, *31*, 2104143.
[11] W. Ahmad, L. Pan, K. Khan, L. Jia, Q. Zhuang, Z. Wang, *Adv. Funct. Mater.* **2023**, *33*, 2300686.
[12] J. Wang, J. Han, X. Chen, X. Wang, *InfoMat* **2019**, *1*, 33.
[13] F. Li, B. Xu, W. Yang, Z. Qi, C. Ma, Y. Wang, X. Zhang, Z. Luo, D. Liang, D. Li, Z. Li, A. Pan, *Nano Res.* **2020**, *13*, 1053.
[14] J. Bullock, M. Amani, J. Cho, Y.-Z. Chen, G. H. Ahn, V. Adinolfi, V. R. Shrestha, Y. Gao, K. B. Crozier, Y.-L. Chueh, A. Javey, *Nat. Photonics* **2018**, *12*, 601.
[15] Y. Chen, Y. Wang, Z. Wang, Y. Gu, Y. Ye, X. Chai, J. Ye, Y. Chen, R. Xie, Y. Zhou, Z. Hu, Q. Li, L. Zhang, F. Wang, P. Wang, J. Miao, J. Wang, X. Chen, W. Lu, P. Zhou, W. Hu, *Nat. Electron.* **2021**, *4*, 357.
[16] Y. Liu, A. Elbanna, W. Gao, J. Pan, Z. Shen, J. Teng, *Adv. Mater.* **2022**, *34*, 2107138.
[17] S. Lukman, L. Ding, L. Xu, Y. Tao, A. C. Riis-Jensen, G. Zhang, Q. Y. S. Wu, M. Yang, S. Luo, C. Hsu, L. Yao, G. Liang, H. Lin, Y.-W. Zhang, K. S. Thygesen, Q. J. Wang, Y. Feng, J. Teng, *Nat. Nanotechnol.* **2020**, *15*, 675.
[18] S. Edelstein, S. R. K. C. Indukuri, N. Mazurski, U. Levy, *Nanophotonics* **2022**, *11*, 4337.
[19] G. Wang, L. Li, W. Fan, R. Wang, S. Zhou, J.-T. Lü, L. Gan, T. Zhai, *Adv. Funct. Mater.* **2018**, *28*, 1800339.
[20] S. Ovesen, S. Brem, C. Linderälv, M. Kuisma, T. Korn, P. Erhart, M. Selig, E. Malic, *Commun. Phys.* **2019**, *2*, 23.
[21] Z. Hu, X. Liu, P. L. Hernández-Martínez, S. Zhang, P. Gu, W. Du, W. Xu, H. V. Demir, H. Liu, Q. Xiong, *InfoMat* **2022**, *4*, e12290.
[22] T. Qi, Y. Gong, A. Li, X. Ma, P. Wang, R. Huang, C. Liu, R. Sakidja, J. Z. Wu, R. Chen, L. Zhang, *Adv. Funct. Mater.* **2020**, *30*, 1905687.
[23] W. Deng, Z. Zheng, J. Li, R. Zhou, X. Chen, D. Zhang, Y. Lu, C. Wang, C. You, S. Li, L. Sun, Y. Wu, X. Li, B. An, Z. Liu, Q. J. Wang, X. Duan, Y. Zhang, *Nat. Commun.* **2022**, *13*, 4627.
[24] C. Yan, L. Gan, X. Zhou, J. Guo, W. Huang, J. Huang, B. Jin, J. Xiong, T. Zhai, Y. Li, *Adv. Funct. Mater.* **2017**, *27*, 1702918.
[25] L. Fu, F. Wang, B. Wu, N. Wu, W. Huang, H. Wang, C. Jin, L. Zhuang, J. He, L. Fu, Y. Liu, *Adv. Mater.* **2017**, *29*, 1700439.
[26] S.-S. Chee, D. Seo, H. Kim, H. Jang, S. Lee, S. P. Moon, K. H. Lee, S. W. Kim, H. Choi, M.-H. Ham, *Adv. Mater.* **2019**, *31*, 1804422.
[27] C. Zhang, C. Gong, Y. Nie, K.-A. Min, C. Liang, Y. J. Oh, H. Zhang, W. Wang, S. Hong, L. Colombo, R. M. Wallace, K. Cho, *2D Mater.* **2016**, *4*, 015026.
[28] Z. Muhammad, R. Islam, Y. Wang, C. Autieri, Z. Lv, B. Singh, P. Vallobra, Y. Zhang, L. Zhu, W. Zhao, *ACS Appl. Mater. Interfaces* **2022**, *14*, 35927.
[29] M. Kim, M. Son, D.-B. Seo, J. Kim, M. Jang, D. I. Kim, S. Lee, S. Yim, W. Song, S. Myung, J.-W. Yoo, S. S. Lee, K.-S. An, *Small* **2023**, *19*, 2206350.
[30] H. Ye, J. Zhou, D. Er, C. C. Price, Z. Yu, Y. Liu, J. Lowengrub, J. Lou, Z. Liu, V. B. Shenoy, *ACS Nano* **2017**, *11*, 12780.
[31] D. Wang, J. Meng, X. Zhang, G. Guo, Z. Yin, H. Liu, L. Cheng, M. Gao, J. You, R. Wang, *Chem. Mater.* **2018**, *30*, 3819.
[32] S. J. Yun, G. H. Han, H. Kim, D. L. Duong, B. G. Shin, J. Zhao, Q. A. Vu, J. Lee, S. M. Lee, Y. H. Lee, *Nat. Commun.* **2017**, *8*, 2163.
[33] S.-S. Chee, W.-J. Lee, Y.-R. Jo, M. K. Cho, D. Chun, H. Baik, B.-J. Kim, M.-H. Yoon, K. Lee, M.-H. Ham, *Adv. Funct. Mater.* **2020**, *30*, 1908147.
[34] B. Zhao, Z. Huo, L. Li, H. Liu, Z. Hu, Y. Wu, H. Qiu, *Nanomaterials* **2023**, *13*, 2520.
[35] J. Ye, K. Liao, X. Ge, Z. Wang, Y. Wang, M. Peng, T. He, P. Wu, H. Wang, Y. Chen, Z. Cui, Y. Gu, H. Xu, T. Xu, Q. Li, X. Zhou, M. Luo, N. Li, M. Zubair, F. Wu, P. Wang, C. Shan, G. Wang, J. Miao, W. Hu, *Adv. Opt. Mater.* **2021**, *9*, 2002248.
[36] D. Wang, X. Zhang, H. Liu, J. Meng, J. Xia, Z. Yin, Y. Wang, J. You, X.-M. Meng, *2D Mater.* **2017**, *4*, 031012.
[37] N. Kang, H. P. Paudel, M. N. Leuenberger, L. Tetard, S. I. Khondaker, *J. Phys. Chem. C* **2014**, *118*, 21258.
[38] S. Kumar, T. Malik, D. Sharma, A. K. Ganguli, *ACS Appl. Nano Mater.* **2019**, *2*, 2651.
[39] Y. Wen, D. Wang, H. Li, W. Jiang, T. Zhou, X. Deng, B. Hu, C. Liu, G. Che, *Appl. Surf. Sci.* **2021**, *567*, 150903.
[40] J. Cho, N. S. Suwandaratne, S. Razek, Y.-H. Choi, L. F. J. Piper, D. F. Watson, S. Banerjee, *ACS Appl. Mater. Interfaces* **2020**, *12*, 43728.
[41] W. Dou, Y. Jia, X. Hao, Q. Meng, J. Wu, S. Zhai, T. Li, W. Hu, B. Song, M. Zhou, *J. Phys. Chem. Lett.* **2021**, *12*, 2682.
[42] D. Ruzmetov, K. Zhang, G. Stan, B. Kalanyan, G. R. Bhimanapati, S. M. Eichfeld, R. A. Burke, P. B. Shah, T. P. O'regan, F. J. Crowne, A. G. Birdwell, J. A. Robinson, A. V. Davydov, T. G. Ivanov, *ACS Nano* **2016**, *10*, 3580.
[43] L. Liu, J. Wu, L. Wu, M. Ye, X. Liu, Q. Wang, S. Hou, P. Lu, L. Sun, J. Zheng, L. Xing, L. Gu, X. Jiang, L. Xie, L. Jiao, *Nat. Mater.* **2018**, *17*, 1108.
[44] A. Azizi, S. Eichfeld, G. Geschwind, K. Zhang, B. Jiang, D. Mukherjee, L. Hossain, A. F. Piasecki, B. Kabius, J. A. Robinson, N. Alem, *ACS Nano* **2015**, *9*, 4882.
[45] H. Jang, Y. Seok, Y. Choi, S.-H. Cho, K. Watanabe, T. Taniguchi, K. Lee, *Adv. Funct. Mater.* **2021**, *31*, 2006788.
[46] K. Xu, Z. Wang, F. Wang, Y. Huang, F. Wang, L. Yin, C. Jiang, J. He, *Adv. Mater.* **2015**, *27*, 7881.
[47] H. Jang, Y. Song, Y. Seok, H. Im, T. H. Kim, J.-H. Lee, Y.-H. Kim, K. Lee, *Nanoscale* **2022**, *14*, 3004.
[48] M. Sun, Q. Fang, D. Xie, Y. Sun, J. Xu, C. Teng, R. Dai, P. Yang, Z. Li, W. Li, Y. Zhang, *Adv. Electron. Mater.* **2017**, *3*, 1600502.

© 2023 The Authors. Advanced Functional Materials published by Wiley-VCH GmbH

16163028, 2024, 7, Downloaded from https://onlinelibrary.wiley.com/doi/10.1002/adfm.202308906 by Ulsan National Institute Of, Wiley Online Library on [23/04/2024]. See the Terms and Conditions (https://onlinelibrary.wiley.com/terms-and-conditions) on Wiley Online Library for rules of use; OA articles are governed by the applicable Creative Commons License

[49] M. Shkir, M. T. Khan, I. M. Ashraf, A. Almohammedi, E. Dieguez, S. Alfaify, *Sci. Rep.* **2019**, *9*, 12436.
[50] J. Yin, Z. Tan, H. Hong, J. Wu, H. Yuan, Y. Liu, C. Chen, C. Tan, F. Yao, T. Li, Y. Chen, Z. Liu, K. Liu, H. Peng, *Nat. Commun.* **2018**, *9*, 3311.
[51] Y. Fang, A. Armin, P. Meredith, J. Huang, *Nat. Photonics* **2019**, *13*, 1.
[52] F. Wang, T. Zhang, R. Xie, Z. Wang, W. Hu, *Nat. Commun.* **2023**, *14*, 2224.
[53] A. Rogalski, *ACS Photonics* **2023**, *10*, 647.
[54] J. Renteria, R. Samnakay, S. L. Rumyantsev, C. Jiang, P. Goli, M. S. Shur, A. A. Balandin, *Appl. Phys. Lett.* **2014**, *104*, 153104.
[55] M. Dai, H. Chen, F. Wang, M. Long, H. Shang, Y. Hu, W. Li, C. Ge, J. Zhang, T. Zhai, Y. Fu, P. Hu, *ACS Nano* **2020**, *14*, 9098.

© 2023 The Authors. Advanced Functional Materials published by Wiley-VCH GmbH

16163028, 2024, 7, Downloaded from https://onlinelibrary.wiley.com/doi/10.1002/adfm.202308906 by Ulsan National Insitute Of, Wiley Online Library on [23/04/2024]. See the Terms and Conditions (https://onlinelibrary.wiley.com/terms-and-conditions) on Wiley Online Library for rules of use; OA articles are governed by the applicable Creative Commons License